# Fluidics Jet Vectoring for Incompressible Flow by Using Counter Flow Method for Circular Duct

**Ali A-M. H. AlAsadi**
Dep. of Mechanical Engineering
College of Engineering
Baghdad University
Email: dralicit@yahoo.com

**Ahmed Hikmat Faseeh**
Dep. of Mechanical Engineering
College of Engineering
Baghdad University
Email: ahf.msc@gmail.com

## Abstract

Computational and experimental investigation of fluidic thrust vectoring using counter-flow method had been carried out in the present work. The experimental investigation involved the design and construction of a test rig for a circular duct to examine the effect of various geometric variables on the thrust vectoring angle. The experimental tests covered Coanda surface radius R/d = (0.58823, 1.17647, 1.75471), secondary gap height h/d = (0.02941, 0.05882), over a secondary mass flow ratio range ($0 \leq \dot{m}_S/\dot{m}_p \leq 0.06568$). Load cell readings were obtained using two components overhead. The computational investigation involved a 3D numerical solution using ANSYS Fluent. The test cases parameters used in the experimental work were used as an input for the numerical solution. The results show that the thrust vectoring angle is increased by increasing the secondary suction rate. Three control zones can be observed: a "dead zone" can be seen at low mass flow ratios. Followed by a control region where continuous primary jet control is achievable until a saturation region is reached. The coanda surface ratio determines the length of the dead zone in which small coanda surface resulted in an extended dead zone region. The secondary gap height increase had an inverse effect on the thrust vectoring angle. The investigation shows that both experimental and computational results obtained followed a similar general pattern and gave a good agreement when compared with available studies on jet vectoring angle.

**Keywords:** Thrust Vectoring, Jet vectoring angle, Coanda effect, Counter-flow, mass flow ratio

## 1. Introduction:

An essential issue concerning performance related operation of any combat aircraft is maneuverability. A maneuver is the result of aircraft response to a control input from the pilot, and it is achieved traditionally by using aerodynamic control surfaces [1]. These surfaces are elevators, canards, rudders and ailerons. When a surface deflects, a change in the aerodynamic moments and forces is produced which causes the aircraft to maneuver [2]. These conventional control systems are inadequate due to limitation by aerodynamic constraints since whenever the aerodynamic forces are small, an effective control is either lost or compromised. In addition, the traditional control methods are heavy, complex in design and require continuous maintenance [1, 2]. As an alternative control method, Thrust Vectoring control (TVC) has established many possible benefits to high performance aircrafts in terms of improved maneuverability, performance and survivability.

Thrust vectoring control is favorable over conventional aerodynamic control for many reasons. Fighting aircrafts' combat efficiency can be increased when multi axis thrust vectoring is added to the aircraft's propulsion system. The aircraft's ability to land and take off from short or damaged runways is also enhanced with the addition of thrust vectoring control since it provides a vertical thrust component that can be added to the lift force produced by the wings [3].

Thrust vectoring control can direct the exhaust thrust of missile or jet engine by various methods. Namely, mechanical thrust vectoring (MTV) which rely on mechanical means for vectoring or the recent methods which are fluidic-based vectoring methods (FTV). In mechanical thrust vectoring, the deflection of nozzle's exhaust thrust of an aircraft is done by mechanical movements driven by pneumatic or hydraulic actuators [4]. Although these methods significantly shortened the take-off and landing distances as well as improving the maneuverability of the aircrafts, they introduced a number of disadvantages [5], since these mechanical flaps and actuators used for vectoring add additional weight and complexity to the fighter jets which in consequence increase the maintenance costs. Due to these disadvantages of the mechanical thrust vectoring, researchers sought to investigate new methods to accomplish the same thrust vectoring requirements without the use of external mechanical parts by fluidically vectoring the jet. i.e Fluidic thrust vectoring [6]

Fluidic thrust vectoring (FTV) is the use of a secondary flow source to control and redirect the exhaust jet of an aircraft without the use of movable parts. The secondary flow is taken from bleed air of an engine fan or compressor [7]. The main advantage of fluidic thrust vectoring control

over its mechanical counterpart is the elimination of movable parts which substantially reduces the weight of the aircraft since large portions of the nozzle geometry could be fixed and integrated with aircraft's structure which permits the elimination of mechanical actuators and kinematic structures [8]. It also provides an enhanced stealth characteristics due to simple tail design [6]. Moreover, Fluidic vectoring techniques offer up to 80% nozzle weight reduction and 50% less maintenance costs in comparison with mechanical control schemes [9]. FTV system depends on the phenomena identified as the Coanda effect.

Coanda effect is a phenomenon discovered by and termed after the Romanian inventor and aerodynamicist Henri-Marie Coanda in 1930, in which the fluid has the inclination to attach itself to a close curved surface due to a reduction in pressure produced by the acceleration of flow around that curved surface. The attachment effect can be controlled by applying a secondary control jet to influence the main jet attachment to the wall [10]. The jet attachment remains even after the surface is curved away from its early direction which is why this effect can be used in changing the primary flow direction. The parameters that affect this phenomenon are secondary slots location and height, the surface radius of curvature, free stream velocity and the secondary stream flow ratio [11].

The fluidic jet vectoring control can be classified into five methods: Synthetic jet actuators, Co-flow, Shock vector control, Counter-flow, and Sonic throat shifting. These methods had been investigated numerically and experimentally with different success levels. The objective of this current work is to conduct a study of the Counter-flow vectoring method for circular nozzle exhaust. The fluidic vectoring concept was proposed by [5]. Jet deflection is accomplished by Vacuum which is generated by secondary counter flow from one of the slots located at the exit of the nozzle close to the primary jet. These slots are fitted with suction collars known as Coanda surfaces. Suction is then applied to secondary flow slot to vector the primary jet flow as an asymmetric pressure is generated by a secondary flow stream at the wall of the coanda collar which influences the primary flow to deflect towards the low-pressure region, [6]. The basic geometry of a CFTV nozzle is illustrated in, **Fig. 1.**

The counter-flow method was investigated numerically and experimentally in this present work. The numerical solution involved solving the fluid flow governing equations using the commercial computational fluid dynamics (CFD) software ANSYS FLUENT 15.0. As for the Experimental work, an investigation of the counter-flow jet vectoring scheme is performed to study the effect of various parameters and the design of multi axis vectoring nozzle which can be driven by a computer to control the primary jet in pitch and yaw directions. Finally, a parametric study was conducted to investigate the effects of several parameters on the jet vectoring angle, such as, Coanda wall radius of curvature (R), Secondary slot gap height (h), and mass flow ratio ($\dot{m}_S/\dot{m}_p$)
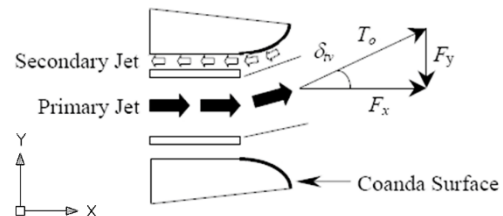


**Figure 1**: Counter-flow jet vectoring concept used in present work [9]

## 2. Computational Simulation:

The Computational solution provides a cheaper alternative way of testing and analyzing complex fluid flow systems without relying on expensive prototyping and cumbersome experimental work measurements. In this work, the numerical solution of the fluidics jet vectoring simulation was done using three dimensional partial differential equations which are based on the conservation of momentum and the conservation of mass, also known The Navier-Stokes equations, and the k-ε turbulence model. The three-dimensional model of the problem was built using CAD software SOLIDWORKS 2015. Then the 3D model was imported to ANSYS Workbench and meshed using ANSYS meshing program, with tetrahedral mesh, **Fig. 3** The computational model of the problem was solved numerically using the commercial CFD code package ANSYS FLUENT 15.0 to analyze the flow field at the exit of the circular nozzle. FLUENT code was chosen due to its comprehensive modeling potentials in solving 3-D fluid flow problems and covers a broad range of turbulent models. The effect of various conada surface geometries and different secondary gap heights were tested. The computational simulation provided the reaction forces data which were compared afterwards with the experimentally obtained data.

### 2.1 Computational Model Geometry:

The system geometry in the present work consists of two zones: Internal volume generated by coanda surface walls outside the circular jet outlet and the room ambient zone. The internal volume generated from coanda walls, primary and secondary openings was generated and then added to the room zone (box) with dimensions: width

(X) = 400 mm, height (Y) = 500 mm, and length (Z)= 700 mm.

The original design geometry consists of primary duct, secondary duct and coanda surface walls. It is similar to the passage generated in the experimental test rig that will be described in in section 3.1. All dimensions aforementioned were based on previous studies [12], [13]. The geometry of the design model is shown in **Fig. 2** The dimensions of these regions of interest are:

1. The primary circular duct outlet with dimensions of d = 34mm
2. The secondary duct with dimensions of length (l) = 50mm, and secondary gap height of h =1 mm and 2 mm respectively.
3. The Coanda wall surface with radius of curvature dimensions of R=20mm, 40mm and 60mm respectively.
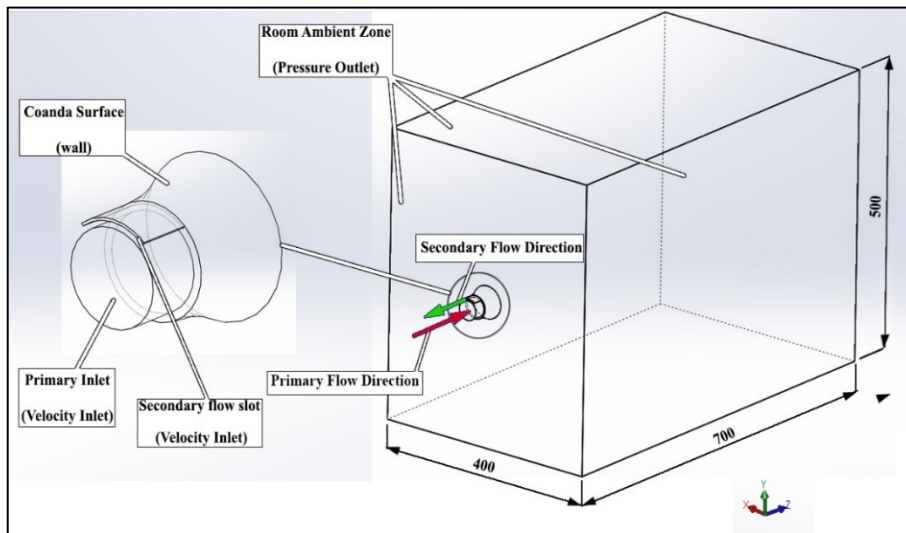


**Figure 2**: Boundary Conditions of the 3D model
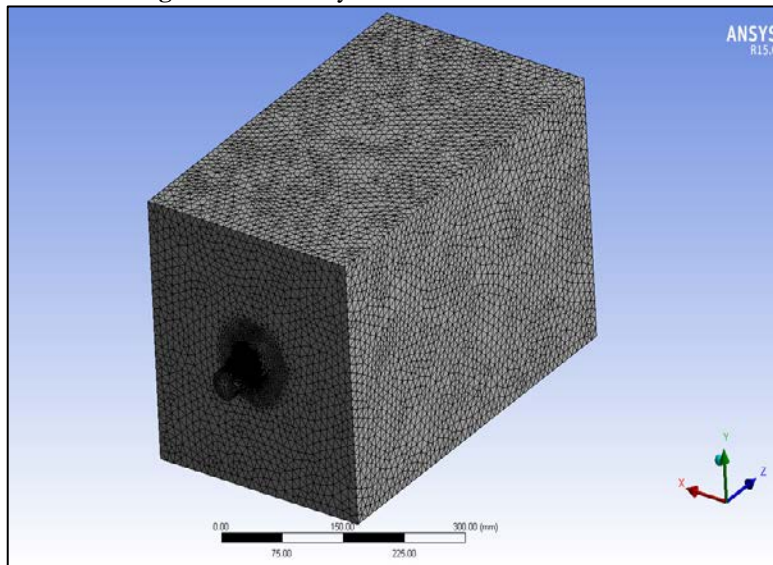


**Figure 3**: Isometric view of the 3D geometry mesh

## 2.2 Assumptions:

The working fluid for this study is Air with constant physical properties. The flow characteristics are assumed to have the following assumptions:
1. Steady flow.
2. Three dimensional.
3. Incompressible flow (low speed flow with main duct velocity $V_p$ = 24 m/s, M < 0.3).

4. Turbulent flow, the values of Reynolds number at primary flow are (60800).
5. No heat source.
6. Atmospheric pressure in all boundaries except in the gap and the collar wall.

## 2.3 Governing Equations:

In this study the numerical solution of steady incompressible flow field equations was done using the ANSYS FLUENT 15.0 built in solver. The governing equations used were the Reynolds

Average Navier Stokes Equations for the continuity and for the momentum equations which are presented in the FLUENT built-in solver are as follows:

**2.3.1 The Conservation of Mass (Continuity) Equation:**

$$\frac{\partial u}{\partial x} + \frac{\partial v}{\partial y} + \frac{\partial w}{\partial z} = 0 \qquad (1)$$

**2.3.2 The Conservation of Momentum Equation:**

For the conservation of momentum equation, it can be written as:

$$\frac{\bar{u}\partial\bar{u}}{\partial x} + \frac{\bar{v}\partial\bar{u}}{\partial y} + \frac{\bar{w}\partial\bar{u}}{\partial z} = -\frac{1}{\rho}\frac{\partial\bar{p}}{\partial x} + \nu(\nabla^2\bar{u}) - \frac{\partial\overline{(\acute{u})^2}}{\partial x} - \frac{\partial\overline{(\acute{u}\acute{v})}}{\partial y} - \frac{\partial\overline{(\acute{u}\acute{w})}}{\partial z}$$

$$(2)$$

$$\frac{\bar{u}\partial\bar{v}}{\partial x} + \frac{\bar{v}\partial\bar{v}}{\partial y} + \frac{\bar{w}\partial\bar{v}}{\partial z} = -\frac{1}{\rho}\frac{\partial\bar{p}}{\partial y} + \nu(\nabla^2\bar{v}) - \frac{\partial\overline{(\acute{u}\acute{v})}}{\partial x} - \frac{\partial\overline{(\acute{v})^2}}{\partial y} - \frac{\partial\overline{(\acute{v}\acute{w})}}{\partial z}$$

$$(3)$$

$$\frac{\bar{u}\partial\bar{w}}{\partial x} + \frac{\bar{v}\partial\bar{w}}{\partial y} + \frac{\bar{w}\partial\bar{w}}{\partial z} = -\frac{1}{\rho}\frac{\partial\bar{p}}{\partial z} + \nu(\nabla^2\bar{w}) - \frac{\partial\overline{(\acute{u}\acute{w})}}{\partial x} - \frac{\partial\overline{(\acute{w}\acute{v})}}{\partial y} - \frac{\partial\overline{(\acute{w})^2}}{\partial z}$$

$$(4)$$

Where $\quad \nabla^2 = \frac{\partial^2}{\partial x^2} + \frac{\partial^2}{\partial y^2} + \frac{\partial^2}{\partial z^2} \qquad (5)$

**2.3.3 Standard k - ε Model Equations:**

Turbulence kinetic energy (k) :

$$\frac{\partial}{\partial t}(\rho k) + \frac{\partial}{\partial x_i}(\rho k u_i) = \frac{\partial}{\partial x_j}\left[\left(\mu + \frac{\mu_t}{\sigma_k}\right)\frac{\partial k}{\partial x_j}\right] + G_k + G_b - \rho\varepsilon - Y_M + S_k \qquad \ldots(6)$$

As for the dissipation of kinetic energy (ε) it can be written as:

$$\frac{\partial}{\partial t}(\rho\varepsilon) + \frac{\partial}{\partial x_i}(\rho\varepsilon u_i) = \frac{\partial}{\partial x_j}\left[\left(\mu + \frac{\mu_t}{\sigma_k}\right)\frac{\partial\varepsilon}{\partial x_j}\right] + C_{1\varepsilon}\frac{\varepsilon}{k}(C_k + C_{3\varepsilon}G_b) - C_{2\varepsilon}\rho\frac{\varepsilon^2}{k} + S_\varepsilon \qquad \ldots(7)$$

**2.4 Boundary Conditions:**

The Boundary conditions importance is to replicate the experimental conditions surrounding the model. In the present work, the boundary conditions specified and illustrated in **Fig. 2** for the current model are:

1- Wall Boundary Condition**:** No-slip boundary condition was assigned for the internal of Coanda wall surface and the walls surrounding the main and secondary flows. This condition used to bound fluid and solid regions.

2- Interior Boundary Condition: The interior boundary condition was appointed to the domain that is bounded by the solid wall and pressure outlet boundary condition.

3- Inlet Velocity Boundary Conditions: This boundary condition is set to inflow velocity of the main duct and have the value of 24 m/s. It was also assigned to the outflow of the secondary flow by assigning a negative value to the secondary flow which inverts flow direction.

4- The solution is initialized with turbulent kinetic energy of k = 2.16 m$^2$/s$^2$ at turbulent dissipation rate of ε = 2874.608 m$^2$/s$^3$ when computed from the main velocity inlet by the FLUENT built-in solver.

**3. Experimental Work:**

The experimental rig was built in the Heat Transfer Lab. At the Mechanical Engineering Dept. _ University of Bagdad. This experimental test rig was built to demonstrate to ability to divert the direction of a main exhaust flow in two axes (pitch and yaw) by the control of a secondary counter flow. The main circular duct is established to provide a stable flow to simulate the exhaust gases from an engine nozzle of unmanned airplane at subsonic speed (24 m/s). As for the secondary flow a circular cylinder with four equally spaced channels parallel to the main flow shrouded the main duct ending. These four slots represent the four direction of vectoring flow (up, down, left, right). A centrifugal blower with flow rate of 11 m$^3$/min was suitable to provide the main jet for the selected outflow velocities. An ejector pump was used as vacuum source for the secondary counter flow. The load cells used were selected to withstand the test section weight and have the sensitivity to measure the jet reaction forces to calculate the vectoring angles. The jet vectoring angle obtained can be calculated as follow:

$$\delta_v = \tan^{-1}\left(\frac{R_Y}{R_X}\right) \qquad (8)$$

A schematic diagram of the experimental rig is shown in **Fig. 4.**

**3.1 Experimental Rig**

The test section shown in **Fig. 5** Consists of a circular duct made from aluminum tube with an outer diameter of 38 mm and an inner diameter of d = 34 mm and length of L= 750 mm. This duct is attached to a centrifugal blower by flexible hose at one end and at the other end is fitted with a peripheral cylinder that introduces the secondary flow. This cylinder has a 73 mm outer diameter and consists of four separate equal channels surrounding the circular duct and parallel to the main flow direction. The four inlets have a constant slot height of 2 mm. The channels outlets are attached to the ejector by four flexible hoses. Furthermore, this cylinder is used to mount different compatible curved collars (Coanda surfaces) to utilize the Coanda effect for fluidic jet vectoring.

Six different collar configurations were studied to examine the effects of changing the collar radius of curvature on the jet vectoring angle. The main dimensions are radius of curvature R=20 mm, 40 mm and 60 mm (R/d= 0.58823, 1.17647, and 1.76471) for two different secondary slot heights h= 1 mm, and 2 mm (h/d= 0.02941, 0.05882). These collars are also made of aluminum with a length of 20mm and 30mm,

outer diameter of Do=73mm and inner diameter of $D_i$= (40mm,42mm) respectively, for the two slot heights. Moreover, the experimental test included ten secondary air mass flows for every collar for the specified main jet velocity. By placing the Coanda collar at the outlet of the

primary nozzle by two screws to the peripheral cylinder and starting a secondary suction air stream, parallel to the Coanda collar wall in the opposite direction of the main flow a counter-flow fluidic jet vectoring can be obtained.
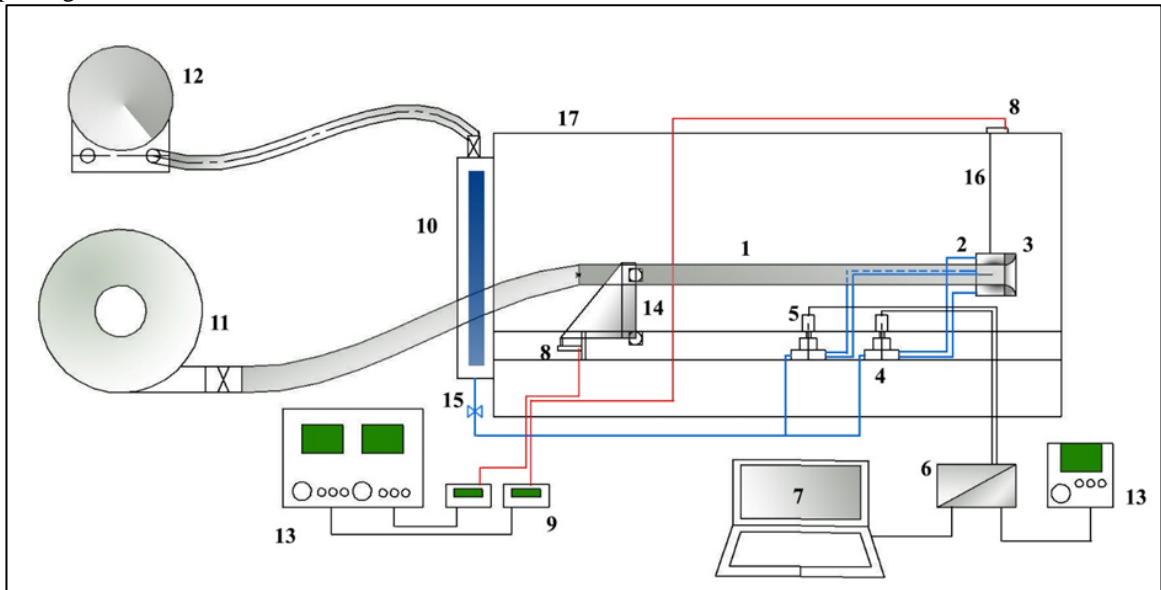


| 1 | Primary Duct (Circular | 7 | Laptop | 13 | Power Supply (2) |
|---|---|---|---|---|---|
| 2 | Secondary flow pipes | 8 | Load Cells (2) | 14 | 1:1 lever and ball bearings |
| 3 | Coanda Collar | 9 | Weight indicator (2) | 15 | Needle valve |
| 4 | Directional Valve (2) | 10 | Air Flow meter | 16 | Chain link |
| 5 | Servo motor (2) | 11 | Centrifugal Blower | 17 | Frame |
| 6 | Arduino Board Control | 12 | Ejector | | |

**Figure 4:** Diagram of the experimental rig
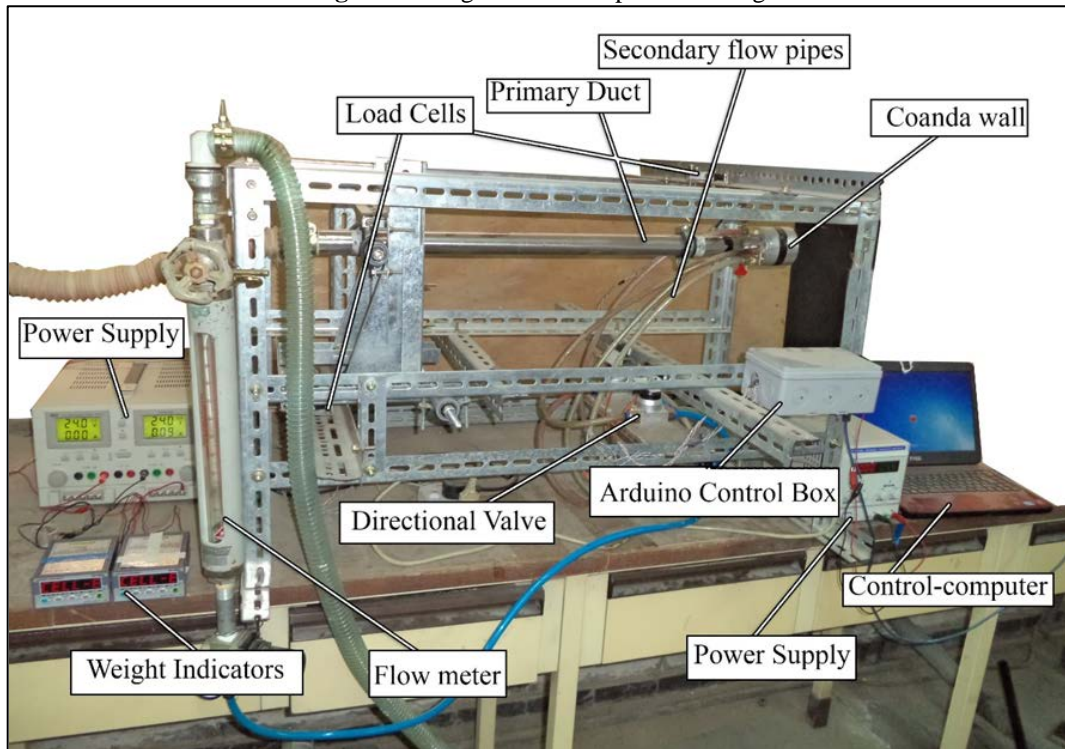


**Figure 5:** Photograph of the experimental rig

### 3.2 Multi Axis Vectoring:

The secondary flow direction is controlled by two modified directional valves. The valves are controlled by two servo motors and an Arduino board. The Arduino is an open-source modeling board based on the ATmega328P microcontroller which can be programmed by a computer integrated development environment (IDE). Arduino boards are capable of reading inputs from sensors, button, serial ports and in turn controlling an output such as motors, lights, relays and other actuators. The Arduino board used in this work was an Arduino UNO R3. It was used to control two servo motors to operate two directional valves.The board was interfaced with the computer through serial port and received its order from a computer program by using the Python programming language. A schematic of the Arduino board valve control is illustrated in **Fig. 6**.
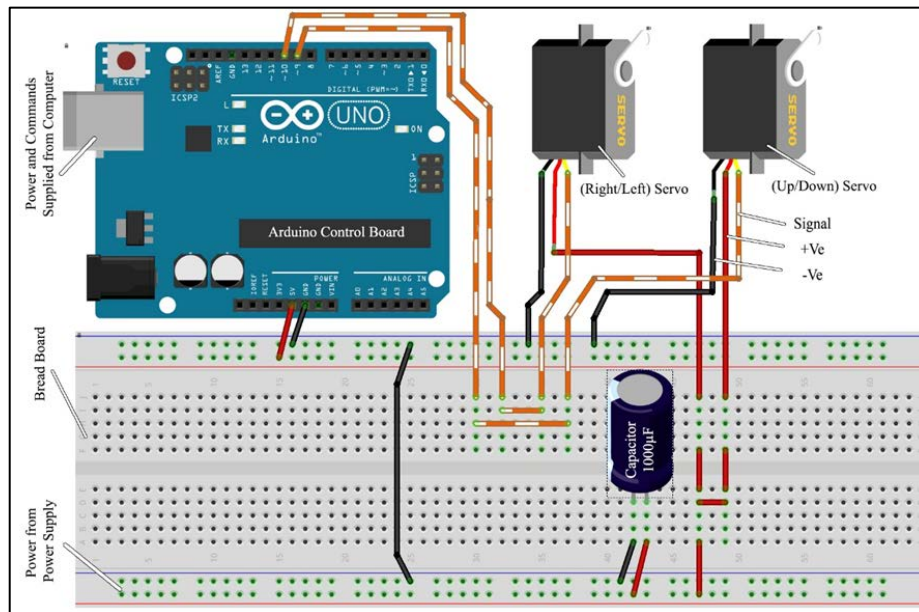


**Figure 6:** Schematic of the Arduino board valve control circuit

## 4. Results and Discussion:

A series of tests were made in order to examine the effects of geometry variables and flow conditions on the jet vectoring angle. These tests included varying Secondary slot height (h), Coanda surface radius of curvature (R) and mass flow ratio ($\dot{m}_S/\dot{m}_p$)

### 4.1 Experimental Results and Discussion:
### 4.1.1 Varying Secondary Gap Height (h/d):

**Fig. 7** shows the relationship between the resulting jet vectoring angle and the mass flow ratio $\dot{m}_S/\dot{m}_p$ for two secondary gap heights at a constant Coanda surface of ratio R/d = 0.58823. The gap heights tested were h/d = 0.02941 and h/d = 0.05882 for the primary flow velocity Vp = 24 m/s. The results show a decrease in the vectoring angle value as the secondary gap height is increased for each mass flow ratio tested. Since the gap height determines the area open for the counter flow stream, increasing the gap height will increase the cross-sectional area of the secondary slot which means a lower secondary velocity for the same mass flow. This increase will yield a lesser secondary slot and collar wall pressure difference with the atmosphere than that of smaller gap heights which leads to less vectoring angle values.
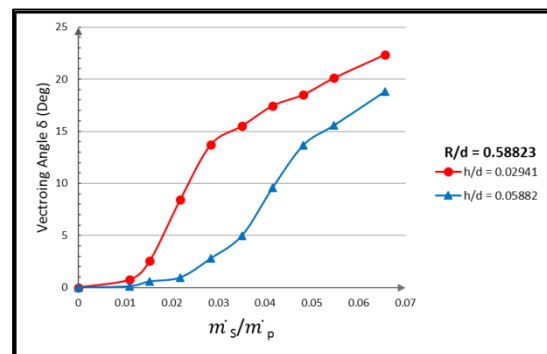


**Figure 7:** Experimental results of Thrust vectoring angle for varying secondary gap height at constant Coanda surface radius R/d = 0.58823

It can also be seen that the thrust vectoring angle value rises as the secondary suction rate is increased. The reason behind this behavior is as the suction flow applied is increased two resulting effects take place at once, the gap pressure decreases which leads to higher secondary flow velocity, and the jet deflection towards the collar walls causes a decrease in the secondary flow area. **Fig. 8** and **9** show the relationship between and the thrust vector angle and $\dot{m}_S/\dot{m}_p$ at constant Coanda surface radius in the range of R/d =

1.17647, 1.76471 respectively. These results show that as the secondary suction flow rate is increased, the thrust vectoring angle value increases. It can be seen that lower vectoring angles values were obtained for the higher secondary gap height at each mass flow ratio tested. In addition, **Fig.** (**7-9**) show that for a smaller gap height the required counter flow is less for the same vectoring angle value which means the attachment can occur for lower amounts of suction levels.
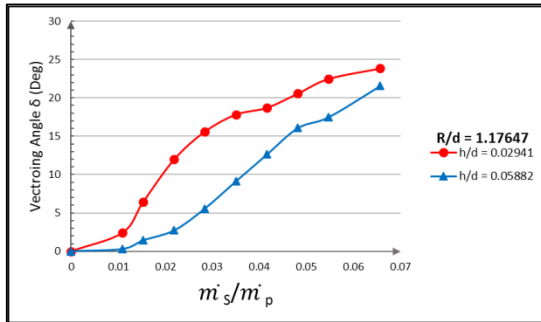


**Figure 8:** Experimental results of Thrust vectoring angle for varying secondary gap height at constant Coanda surface radius R/d = 1.17647
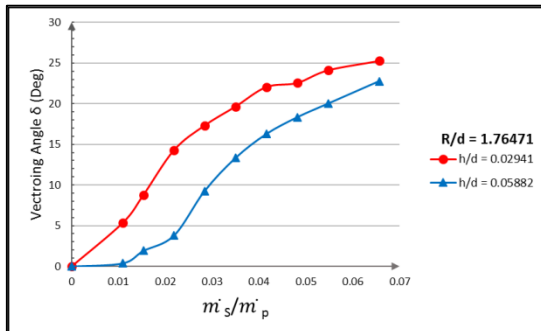


**Figure 9:** Experimental results of Thrust vectoring angle for varying secondary gap height at constant Coanda surface radius R/d = 1.76471

In **Fig.** (**7-9**) The results showed that at very low secondary suction rates $\dot{m}_S \ll \dot{m}_p$, the vectoring angles formed were very small which developed what appears to be a "dead zone" where adequate flow control cannot be achieved. This condition can be based on the fact that the Coanda effect cannot function at low secondary suction rates because at low suction rates, an early separation of secondary jet from the Coanda wall occurs. Faster flowing primary jet will entrain the slower secondary flow which rather than adhering to the Coanda collar wall and remain attached farther downstream separates and generates a higher-pressure region. After the "dead zone", Coanda effect takes over and the curve enters a region where greater thrust vectoring angles can be obtained for moderately smaller increases in the mass flow rates. This region insures a continuous control of the primary jet until the thrust vectoring angle and consequently the thrust vector force produced will arrive at a hypothetical

region of saturation where the thrust vector angle reaches a nearly constant value, for any increase in the mass flow ratio. This trend is shown schematically in **Fig. 10.**
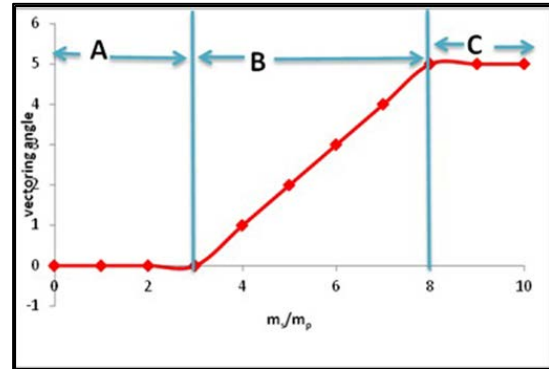


**Figure 10:** Trend line of the experimental results: A – Dead zone, B – Active control, C – Saturation

### 4.1.2 Varying Coanda Surface Radius (R/d):

The resultant thrust vectoring angles have been obtained at various mass flow ratios ($\dot{m}_S/\dot{m}_p$) for three Coanda wall radii. **Fig. 11** and **12** represent the relationship between thrust vectoring angle and $\dot{m}_S/\dot{m}_p$ for constant gap height of h/d = 0.02941 and h/d = 0.05882 at different Coanda surface radius R/d = 0.58823, 1.17647, and 1.76471 for primary flow velocity Vp = 24 m/s. The results showed that as the mass flow rate ratio is increased, the thrust vector angle value increases.
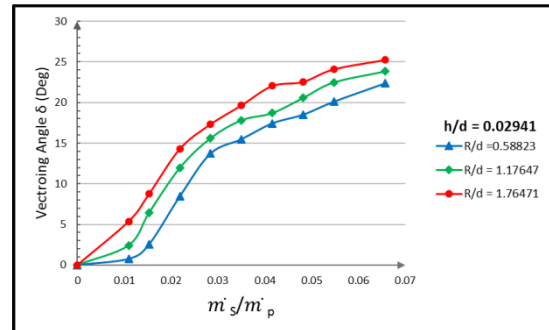


**Figure 11:** Experimental results of Thrust vectoring angle for varying Coanda surface radius at constant secondary gap height h/d = 0.02941
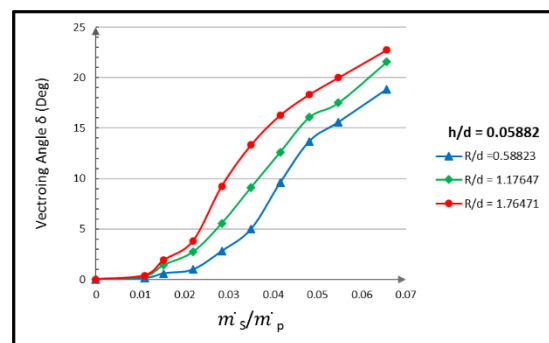


**Figure 12:** Experimental results of Thrust vectoring angle for varying Coanda surface radius at constant secondary gap height h/d = 0.05882

As can be seen from **Fig. 11.** the thrust vectoring angle value increases proportionally with the increase of Coanda wall radius for each mass flow ratio tested because increasing collar length enlarges the area on the which the gauge collar pressure distribution can act upon. Larger radii of Coanda collars provide larger surfaces for the fluid to attach to and the generated pressure difference is higher than that generated from smaller Coanda radius which in turn increases the normal collar force and as a result, a greater thrust vectoring angle can be achieved. Also, with the increase of Coanda surface radius the slope of the curve becomes steeper once it overcomes the "dead zone". The Coanda surface radius affects the size of the "dead zone" as well, and as a consequence where the control region begins. The results showed for smaller mass flow ratios the jet is more likely to separate for a smaller radius of Coanda surface and therefore the "dead zone" will be extended over a wider range of secondary suction rate values.

### 4.2 Computational Results:

The commercial CFD package ANSYS FLUENT 15.0 3D had been used to simulate the experimental results where six cases of the experimental work have been tested for two different gap height ratios and three Coanda surface radius ratios. The results were presented as contours of velocity magnitude, static pressure contours. The data gathered from FLUENT to find $R_Y$ and $R_X$ forces to estimate the thrust vectoring angle. **Fig. 13a** shows the contour of velocity magnitude for a non-vectored primary jet, $\dot{m}_S/\dot{m}_p = 0$ and **Fig. 13b.** show the contour colored by velocity magnitude for a vectored jet where R/d =1.76471, h/d = 0.02941, $\dot{m}_s/\dot{m}_p = 0.06568$. In this case, the upper secondary jet slot was activated in order to vector the primary jet.

It can be seen that the entrainment on the upper Coanda surface has been inhibited during vectoring and the regions of re circulating flow on the Coanda surface. Also, the velocity contour show velocity distribution at primary, secondary ducts and near the Coanda surface. **Fig. 14.** shows the contour of static pressure. In the pressure contours, the clearest point is the low pressure region near Coanda surface due to high speed of secondary flow which responsible for vectoring primary jet.

### 4.1 Varying Secondary Gap Height (h/d):

**Fig. (15-17)** show the numerical results between jet vector angle and the mass flow ratio for different secondary gap heights at constant Coanda surface ratio of R/d = 0.58823, R/d = 1.17647 and R/d =1.76471 respectively. Two secondary gap heights were tested in the range of h/d = 0.02941 and h/d = 0.05882. The results showed an increase in thrust vectoring angle value as the secondary suction rate is increased and as

the secondary gap height ratio was increased, it led to a decline in vectoring angle value for each mass flow ratio tested.
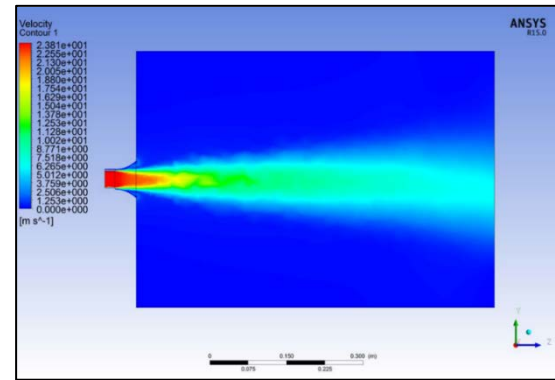


(a) Non-vectored jet $\dot{m}_s/\dot{m}_p = 0$
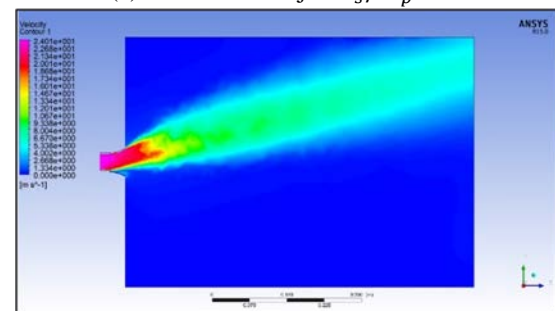


(b) R/d = 1.76471, h/d = 0.02941, $\dot{m}_s/\dot{m}_p = 0.06568$

**Figure 13:** Contours of velocity magnitude
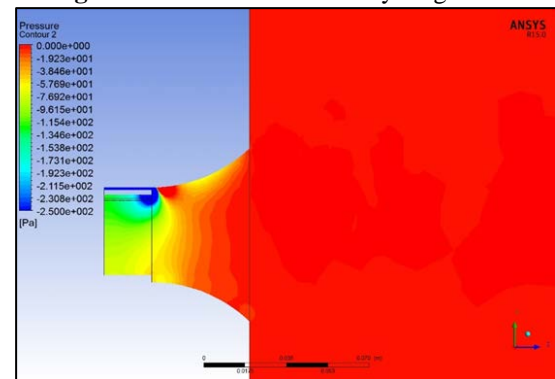


R/d =1.76471, h/d = 0.02941, $\dot{m}_s/\dot{m}_p = 0.06568$

**Figure 14:** Static pressure contour
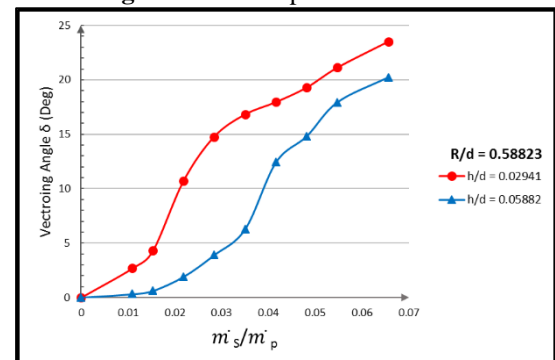


**Figure 15:** Numerical results of Thrust vectoring angle for varying secondary gap height at constant Coanda surface radius R/d = 0.58823
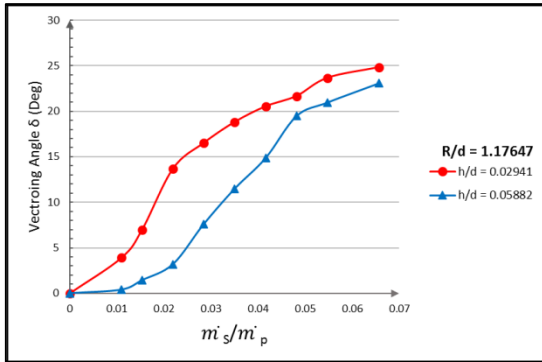
**Figure 16:** Numerical results of Thrust vectoring angle for varying secondary gap height at constant Coanda surface radius R/d = 1.17647
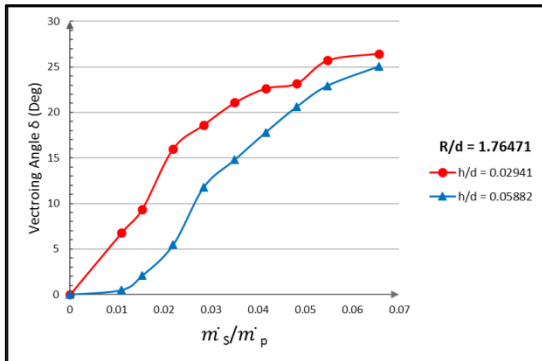


**Figure 17:** Numerical results of Thrust vectoring angle for varying secondary gap height at constant Coanda surface radius R/d = 1.76471

### 4.2 Varying Coanda Surface Radius (R/d):

**Fig. 18** and **Fig. 19** shows the relationship between the jet vectoring angle and mass flow ratio at different Coanda surface ratios at constant secondary gap height ratio of h/d = 0.02941 and h/d = 0.05882. Three Coanda surface ratios were tested, R/d = 0.58823, 1.17647 and 1.76471. The results showed that as the suction rate is increased, the thrust vectoring angle increases. And by increasing the Coanda surface radius, the thrust vectoring values obtained increases accordingly for each tested mass flow ratio.
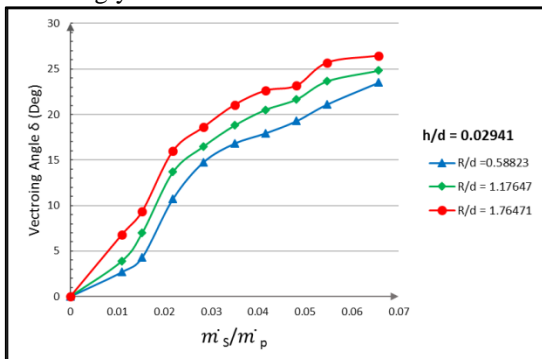


**Figure 18:** Numerical results of Thrust vectoring angle for varying Coanda surface radius at constant secondary gap height h/d = 0.02941
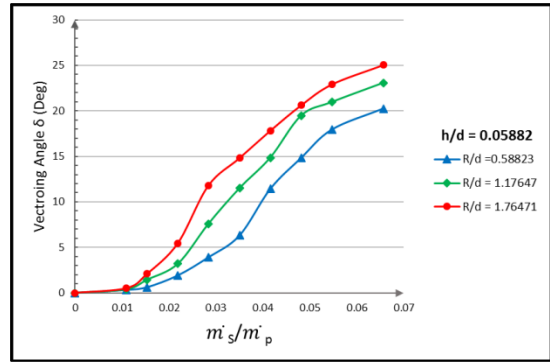


**Figure 19:** Numerical results of Thrust vectoring angle for varying Coanda surface radius at constant secondary gap height h/d = 0.05882

## 5. Smoke Flow Visualization:

**Fig. 20a** shows the visualization of a non-vectored primary jet for R/d =1.76471, h/d = 0.02941, $\dot{m}_s/\dot{m}_p$ = 0. **Fig. 20b** shows the visualization of a vectored primary jet for Coanda surface radius ratio of R/d = 1.76471 and $\dot{m}_S/\dot{m}_p$ = 0.06568 at constant secondary gap height ratio of h/d = 0.02941. The smoke visualization in **Fig. 20** demonstrated a positive pitch vectoring control achieved by controlling the secondary slot flow automatically using a directional valve controlled by the Arduino control board that receives its orders from computer interface to simulate a flight envelope.
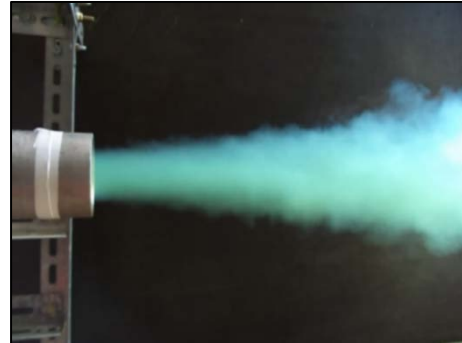


(a) Non-vectored primary flow, R/d =1.76471, h/d = 0.02941, $\dot{m}_s/\dot{m}_p = 0$



(b) Vectored primary flow, R/d =1.76471, h/d = 0.02941, $\dot{m}_s/\dot{m}_p = 0.06568$

**Figure 20:** Smoke visualization of a vectored and non-vectored primary jet

## 6.Verification of Results:

The experimental and numerical results for has been plotted and compared with each other, as shown in **Fig. 21** and **Fig. 22.**

The experimental parameters have been used in FLUENT to obtain the numerical results for test cases of the experiment. These figures show that the numerical and experimental results follow a similar trend. However, the range of the "dead zone" for the experimental work is more extended than that obtained for the theoretical work. Also, the saturation and control regions were highlighted by computational work same as the experimental work. It can be seen that for the same mass flow ratios, the thrust vectoring angle values predicted from CFD results were greater than those obtained from the experimental tests. This difference between numerical and experimental data is due to irregularities in secondary slot plumbing and Coanda collar machining in the experimental model that were impossible to replicate in the computational model. A comparison was made with the results achieved from previous studies to verify the results obtained from the present study. The present results for the effect of varying secondary gap height on thrust vectoring angle at constant Coanda surface radius shown in **Fig. (7-9)** are in good agreement with the results of (the experimental and numerical work) of [14] shown in **Fig.23,** and with (the experimental and numerical work) [12] in **Fig. 24.**

The present results for the effect of varying Coanda surface ratio on thrust vectoring angle at constant secondary gap height shown in **Fig. 11** and **Fig. 12** agree with the following previous works (the experimental and numerical work [13] shown in **Fig. 25** and with (the experimental and numerical work [14] shown in **Fig. 26**.
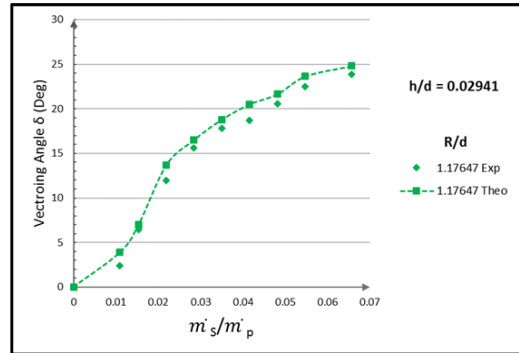


(b) h/d = 0.02941, R/d = 1.17647
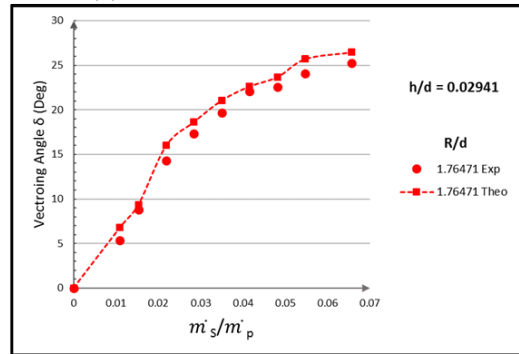


(c) h/d = 0.02941, R/d = 1.76471

**Figure 21:** Comparison between theoretical and experimental results for varying Coanda radius at constant secondary gap height h/d =0.02941
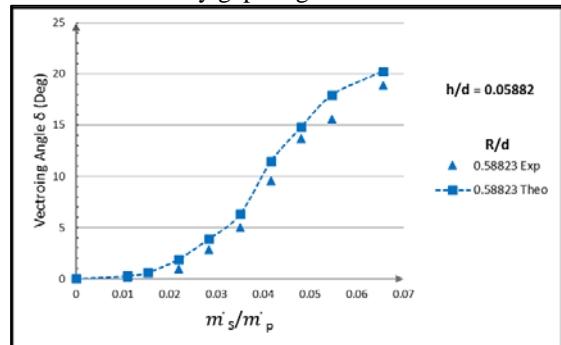


(a) h/d = 0.05882, R/d = 0.58823



(a) h/d = 0.02941, R/d = 0.58823
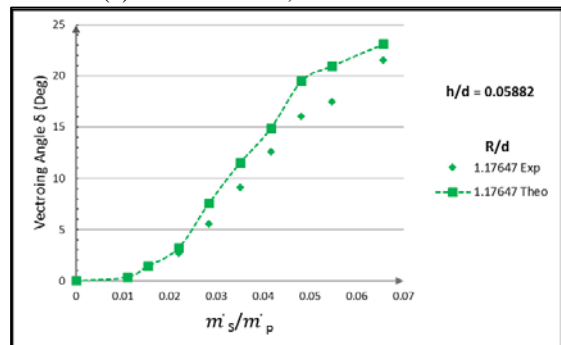


(b) h/d = 0.05882, R/d = 1.17647
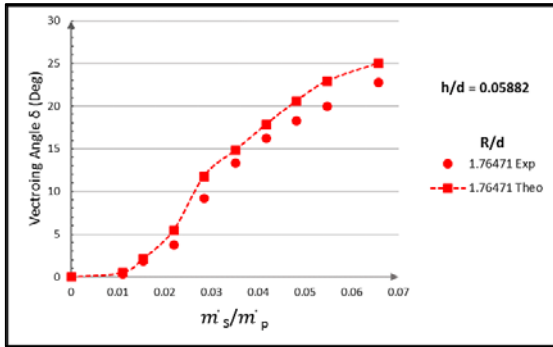
(c) h/d = 0.05882, R/d = 1.76471

**Figure 22:** Comparison between theoretical and experimental results for varying Coanda radius at constant secondary gap height h/d =0.05882
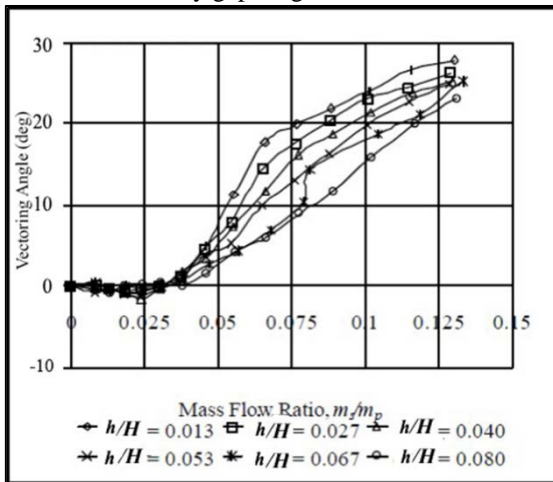


**Figure 23:** Experimental results [14]
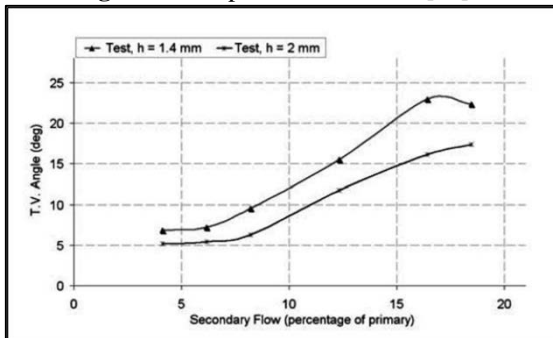


**Figure 24:** Experimental results [12]
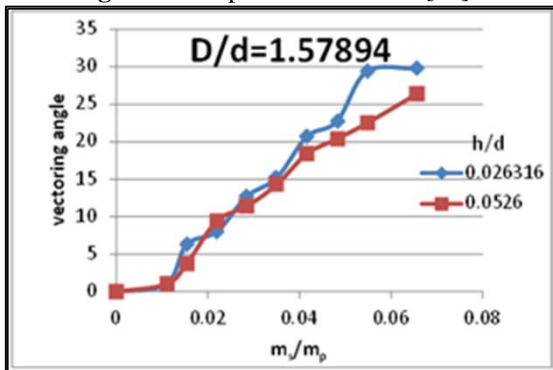


**Figure 25:** Experimental results [13]
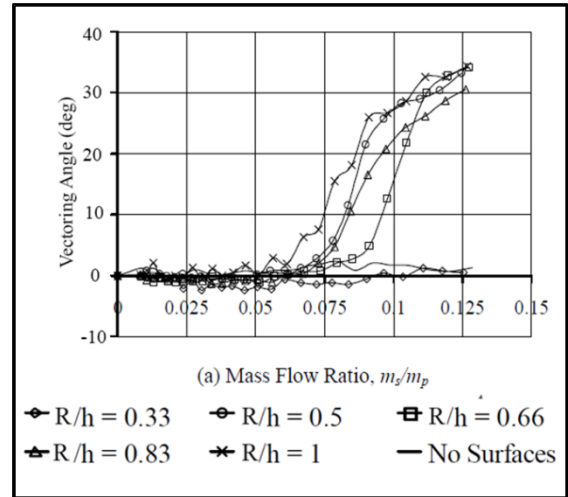


**Figure 26:** Experimental results [14]

## 7. Conclusions:

Fluidic jet vectoring using counter-flow method at subsonic flow have been investigated numerically and experimentally in this present work.

The computational and experimental results obtained from present work followed a similar trend line: Three regions can be observed from the relationship relating jet vectoring angle and mass flow ratio. A 'dead zone' appeared at low secondary mass flowrates where the thrust vectoring angle measured was small and an adequate thrust vectoring control was not possible. Followed by an active control region in which a continuous jet vectoring control can be achieved. Last, a hypothetical saturation region is then formed where the thrust vectoring angle value nearly remained constant for any further increase in secondary suction rate. the vectoring angle value increased by increasing the mass flow ratio, and coanda surface radius once the dead zone has been overcome. The size of radius of curvature of the coanda surface determined the length of the dead zone. A small surface radius resulted in an extended region of the dead zone. The secondary gap height has an inverse effect on the thrust vectoring angle. The thrust vectoring angle was decreased by increasing the secondary gap height for each mass flow ratio tested. Finally, an effective multi-axis control of the primary jet was possible for the current exit nozzle design. Vectoring control was performed automatically using directional valves controlled by an Arduino Uno board through computer interface to simulate a flight envelope which was demonstrated by smoke visualization.

## 8. References:

[1] M. M. Santos, "Experimental Study on Counterflow Thrust Vectoring of a Gas Turbine

Engine," Ph.D. Dissertation, Florida State University, Florida, USA, 2005.

[2] T.M. Ragab, and B. Elhadidi, "Counter Flow Fluid Thrust Vector Applied to Small Business Jets," 13th International Conference: Aerospace Sciences and Aviation Technology, Cairo, Egypt, pp. 1-13, 2009.

[3] J.D. Flamm, "Experimental Study of a Nozzle Using Fluidic Counterflow for Thrust Vectoring", 34th AIAA/ASME/SAE/ASEE Joint Propulsion Conference and Exhibit, Cleveland, Ohio, July 13-15, AIAA 98-3255, 1998.

[4] D. Ikaza, "Thrust Vectoring Nozzle for Military Aircraft Engines," International Congress; 22nd, International Council of The Aeronautical Sciences, Madrid, Spain, pp. 1-10, 2000.

[5] P.J. Strykowski, A. Krothapalli, "Vectoring Thrust Using Confined Shear Layers," Naval Research Reviews, vol. 51, no. 3, pp. 26-34, 1999.

[6] L. Li, M. Hirota, T. Saito, "Numerical and Experimental Studies of Fluidic Thrust Vectoring," International Symposium on Shock Waves (ISSW), Manchester, UK, pp. 2-7, 2011.

[7] K.A. Deere, B.L. Berrier, J.D. Flamm, S.K Johnson, "A Computational Study of a New Dual Throat Fluidic Thrust Vectoring Nozzle Concept," 41st AIAA/ASME/SAE/ASEE Joint Propulsion Conference & Exhibit, 10-13 July, Tucson, Arizona, AIAA Paper., vol. 3502, pp. 1-16, 2005.

[8] D. J. Wing, V. J. Giuliano, "Fluidic Thrust Vectoring of an Axisymmetric Exhaust Nozzle at Static Conditions," ASME Fluids Engineering Division Summer Meeting, FEDSM97-3228, June 22 - 26, 1997.

[9] K. A. Deere, "Summary of Fluidic Thrust Vectoring Research Conducted at NASA Langley Research Center," 21st AIAA Applied Aerodynamics Conference, Fluid Dynamics and Co-located Conferences. Conference Paper, June, pp. 1-18, 2003.

[10] C. Olivotto, "Fluidic Elements Based on Coanda Effect," Incas Bulletin, vol. 2, no. 4, pp. 163-172, 2010.

[11] "Coanda Effect" [website]: https://www.thermofluids.co.uk/effect.php.

[12] A. Banazadeh, F. Saghafi, M. Ghoreyshi, P. Pilidis, "Experimental and Computational Investigation into The Use of Co-Flow Fluidic Thrust Vectoring on A Small Gas Turbine." The Aeronautical Journal, vol.112, no.1127, pp.17-25. 2008.

[13] H. H. Salih, "Theoretical and Experimental Study of Fluidic Jet Vectoring in Subsonic Flow for Circular Nozzle using Co-flow Method," MSc. Thesis, University of Baghdad, College of Engineering, Iraq, 2015.

[14] M. S. Mason, W. J. Crowther, "Fluidic Thrust Vectoring of Low Observable Aircraft," In CEAS Aerospace Aerodynamic Research Conference, pp. 1–7. 2002.

**Nomenclature:**

| Symbol | Definition | Units |
|---|---|---|
| d | Diameter of Primary Jet | mm |
| h | Secondary Gap Height | mm |
| $\dot{m}_p$ | Primary Mass flow rate | Kg/s |
| $\dot{m}_S$ | Secondary Mass Flow Rate | Kg/s |
| R | Coanda surface Radius of curvature | mm |
| Re | Reynolds number | |
| Rx | Horizontal reaction Force | kg |
| Ry | Vertical reaction Force | kg |
| $\bar{u}$ | Average Velocity in x Axes | m/s |
| $\acute{u}$ | Fluctuations Velocity in x Axes | |
| $\bar{v}$ | Average Velocity in y Axes | m/s |
| $\acute{v}$ | Fluctuations Velocity in y Axes | |
| $\bar{w}$ | Average Velocity in z Axes | m/s |
| $\acute{w}$ | Fluctuations Velocity in z Axes | |
| $G_k$ | The generation of turbulence kinetic energy due to the mean velocity gradients = $-\rho\overline{\acute{u}_i\acute{u}_j}\frac{\partial u}{\partial x_j}$ | |
| $G_b$ | The creation of turbulence kinetic energy as a result of buoyancy = $\beta g_i \frac{\mu_t}{Pr_t}\frac{\partial T}{\partial x_i}$ | |
| $S$ | The modulus of the mean rate-of-strain tensor = $\sqrt{2S_{ij}S_{ij}}$ | |
| $Y_M$ | The dilatation dissipation = $2\rho\varepsilon\left(\frac{k}{a^2}\right)^2$ | |
| $\mu_t$ | The turbulent viscosity | |
| $\delta_v$ | Jet vectoring angle | degree |
| $\rho$ | Density | Kg/m$^3$ |
| CFD | Computational Fluid Dynamics | |
| FTV | Fluidic thrust vectoring | |
| CFTV | Counter flow thrust vectoring | |
| MTV | Mechanical thrust vectoring | |
| 3-D | Three dimensional | |
| $V_p$ | Velocity of the primary flow | m/s |
| X | Width of Box Model in ANSYS FLUENT | mm |
| Y | Height of Box Model in ANSYS FLUENT | mm |
| Z | Length of Box Model in ANSYS FLUENT | mm |

# توجيه مائع نفاث باستخدام طريقة الجريان المعاكس لتدفق لا انضغاطي لمنفذ دائري المقطع

**احمد حكمت فصيح**

قسم الهندسة الميكانيكية

جامعة بغداد

**علي عبد المحسن الاسدي**

قسم الهندسة الميكانيكية

جامعة بغداد

**الخلاصة**

تضمن البحث الحالي دراسة عملية ونظرية لتوجيه نفاث رئيسي باستخدام طريقة دفع نفاث ثانوي معاكس لاتجاه النفاث الرئيسي. شمل الجانب العملي تصميم و بناء منظومة اختبار متكونة من قناة نفث دائرية المقطع تنفث المائع الرئيسي لدراسة تأثير المتغيرات الهندسية المختلفة المؤثرةعلى مقدار زاوية توجيه المائع الرئيسي. مثل نصف قطر سطح الانحناء (R/d) = (0.058823,1.17647,1.75471), ارتفاع الفتحة الثانوية (h/d) =(0.05882, 0.02941) و نسبة التدفق الكتلي للمائع الثانوي الى المائع الرئيسي ($\dot{m}_s/\dot{m}_p$) والذي تراوحت مابين 0 ≤ $\dot{m}_s/\dot{m}_p$ ≥ 0.07882 وقد تم الحصول على قياسات مقدار متجه النفث العمودية والافقية باستخدام اثنين من اجهزة قياس الوزن (load cells). اما بالنسبة للجانب النظري فقد تم عمل محاكاة ثلاثية الابعاد للجريان باستخدام البرنامج التجاري ANSYS FLUENT 15.0 و استخدمت حالات الاختبار العملية كمدخلات للحل العددي. أظهرت النتائج أن مقدار زاوية توجيه النفاث تزداد نسبيا عن طريق زيادة معدل الجريان الثانوي.هناك ثلاث مناطق تحكم يمكن ملاحظتها: :وجود "منطقة ميتة" عند نسب التدفق الكتلي المنخفضة و التي لا يمكن أن يتحقق السيطرة على التوجيه فيها. تليها منطقة السيطرة المستمرة حيث يتحقق التحكم بالنفاث الرئيسي حتى يتم الوصول إلى منطقة التشبع. يحدد قطر السطح المنحني مدى امتداد المنطقة الميتة والتي يزداد مقدارها عندما يكون نصف القطر صغيرا. ايضا تم ملاحظة ان زيادة ارتفاع الفجوة الثانوية له تأثير عكسي على مقدار زاوية التوجيه. أظهر التحقيق أن النتائج التجريبية والنظرية التي تم الحصول عليها تتبع نمطا مماثل مع وجود اتفاق جيد بعد مقارنتها مع الدراسات السابقة لزاوية توجيه النفاث.

**الكلمات المفتاحية:** توجيه نفاث, زاوية توجيه نفاث, ظاهرة السطح المنحني, الجريان المتعاكس, معدل التدفق الكتلي